Journal of Medicinal Chemistry

Article

pubs.acs.org/jmc

Discovery of 1,2,3-Triazole Derivatives for Multimodality PET/CT/Cryoimaging of Myelination in the Central Nervous System

Chunying Wu,[*,†] Brendan Eck,[§] Sheng Zhang,[†] Junqing Zhu,[†] Anand Dev Tiwari,[†] Yifan Zhang,[§] Yunjie Zhu,[†,¶] Jinming Zhang,[‖] Bin Wang,[⊥] Xizhen Wang,[⊥] Xu Wang,[⊥] Jingqiang You,[‡] Jian Wang,[#] Yihui Guan,[▽] Xingdang Liu,[▽] Xin Yu,[§] Bruce D. Trapp,[◆] Robert Miller,[○] Jerry Silver,[‡] David Wilson,[§] and Yanming Wang[*,†,⊥]

[†]Department of Radiology, [‡]Department of Neuroscience, [§]Department of Biomedical Engineering, Case Western Reserve University, 11100 Euclid Avenue, Cleveland, Ohio 44106, United States,

[‖]Department of Nuclear Medicine, PLA General Hospital, Beijing 100853, China

[⊥]Department of Radiology, Bingzhou Medical University, Binzhou, Shandong 256603, China

[#]Department of Neurology, [▽]Department of Nuclear Medicine, Huashan Hospital, Shanghai, 200040, China

[○]Department of Anatomy and Regenerative Biology, George Washington University, Washington, D.C. 20037, United States

[◆]Department of Neurosciences, Cleveland Clinic, Cleveland, Ohio 44195, United States

Supporting Information

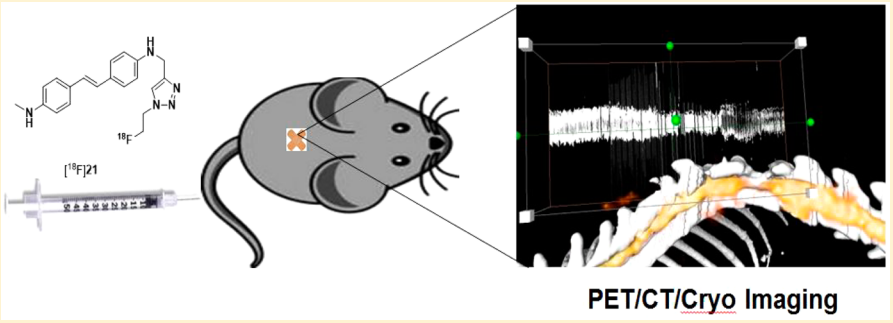

ABSTRACT: Myelin pathology is present in many neurological conditions such as multiple sclerosis (MS) and traumatic spinal cord injury (SCI). To facilitate development of novel therapies aimed at myelin repair, we set out to develop imaging agents that permit direct quantification of myelination in vivo. In this work, we designed and synthesized a series of fluorescent fluorinated myelin imaging agents that can be used for in vivo positron emission tomography (PET) imaging combined with subsequent post-mortem fluorescent cryoimaging. Structure−activity relationship (SAR) studies of the newly developed myelin imaging agents led us to identify a lead compound (TAFDAS, **21**) that readily enters the brain and spinal cord and selectively binds to myelin. By conducting sequential PET and 3D cryoimaging in an SCI rat model, we demonstrated for the first time that PET and cryoimaging can be combined as a novel technique to image the spinal cord with high sensitivity and spatial resolution.

INTRODUCTION

Myelin membranes constitute an insulating layer around axons which allow electrical impulses to transmit quickly and efficiently along the nerve cell.[1,2] Abnormalities or destruction of myelin (demyelination) occurs in many neurodegenerative conditions such as multiple sclerosis (MS)[3,4] and traumatic injury of the spinal cord.[5] In the United States alone, an estimated 350000 people are afflicted by MS and over 10000 spinal cord injuries (SCIs) occur every year. Tremendous efforts are being made to develop novel therapeutic agents to prevent demyelination and/or promote remyelination. For efficacy evaluation of myelin-repair therapies, myelin-specific imaging tools are needed for longitudinal evaluation and quantification of myelin in vivo.

Currently, conventional magnetic resonance imaging (MRI) is widely used to detect lesions formed in the brain and spinal cord.[6−9] However, the use of MRI as a primary measure of disease activity is only indirectly related to clinical outcome. This is due to the fact that MRI relies solely on changes of diffusivity of water to detect lesions, which is a nonspecific measure of the overall changes in macroscopic tissue injury that ranges from edema to inflammation, demyelination, and axonal loss. Thus, MRI does not provide a direct measure of myelin content to specifically detect and quantify demyelination or remyelination,

Received: September 9, 2016

DOI: 10.1021/acs.jmedchem.6b01328
J. Med. Chem. XXXX, XXX, XXX−XXX

Scheme 1. Click Synthesis of Fluorinated MeDAS Analogues (18−23)[a]

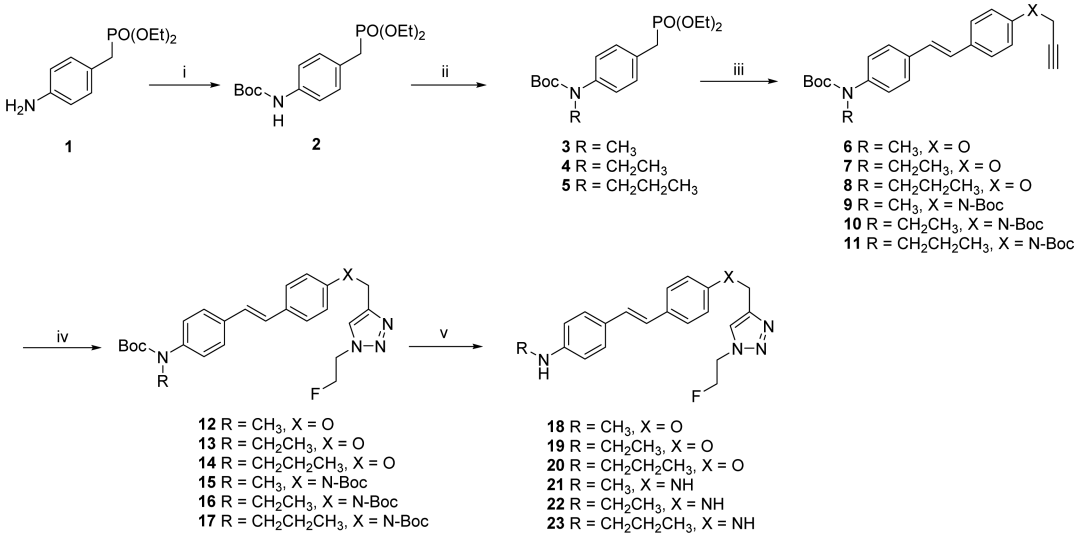

[a](i) Boc_2O, THF; (ii) R-I, NaH, THF; (iii) NaH, 4-(prop-2-yn-1-yloxy)benzaldehyde or *tert*-butyl (4-formylphenyl) (prop-2-yn-1-yl)carbamate (**24**), DMF; (iv) 1-azido-2-fluoroethane, CuI, Et_3N, DMF, MeOH; (v) HCl, H_2O, NaOH.

To overcome the limitations of MRI, we have demonstrated the feasibility to directly detect and quantify myelin changes in the central nervous system (CNS) based on positron emission tomography (PET), which is a functional imaging modality widely used in clinical settings with high sensitivity and quantitation capability. Over the past decade, we have developed a wide array of myelin-specific radiotracers based on different pharmacophores.[10−19] Using a C-11 labeled radiotracer, [^{11}C]MeDAS, we have demonstrated proof-of-principle for using PET as an imaging end point for monitoring treatment response for myelin-repair therapies.[18] To further enhance its potential for routine clinical use, we set out to develop fluorinated analogues of MeDAS, which potentially can be radiolabeled with fluorine-18 and distributed by a central radiopharmacy and used in medical facilities that are not equipped with an on-site cyclotron. Our studies showed that selected compounds readily entered the brain and selectively bound to myelin.[19] To further optimize the pharmacokinetic profiles and achieve rapid, reliable, and reproducible F-18 labeling, we designed and synthesized a novel series of fluorinated and fluorescent compounds using click chemistry through Cu(I)-catalyzed Huisgen cycloaddition. In this work, we report the design, synthesis, and imaging studies of a series of fluorinated triazole analogues of MeDAS. Systematic structure−activity relationship (SAR) studies led us to identify a lead compound termed TAFDAS (**21**) that can be used for both in vivo PET imaging and subsequent post-mortem 3D cryoimaging. We hypothesize that, using the same imaging agent, PET can be coregistered with microscopic 3D cryoimaging to seamlessly combine the unique features of quantitative physiologic information provided by PET with microscopic histologic information in high resolution provided by cryoimaging.

RESULTS

Chemical Synthesis. A series of fluorinated triazole derivatives of MeDAS with different *N*-alkyl groups were designed and synthesized as shown in Scheme 1. Incorporation of triazole provides a pharmacophore that can be readily synthesized and radiolabeled through a click reaction. Currently, the most common method of F-18 labeling is the direct nucleophilic substitution of sulfonic acid esters (such as tosylates, triflates, or mesylates) into the precursor with fluorine-18, but this reaction condition raises the possibility of side reactions like E-2 elimination and substitution of other potential leaving groups. Over the past decade,[20−23] a 1,3-dipolar cycloaddition reaction between alkynes and azides has been widely applied to radiolabeling with high specificity and good yields, which thereby allows efficient F-18 labeling of radiopharmaceuticals.

As shown in Scheme 1, the synthesis starts with Boc protection of the amino group of compound diethyl (4-aminobenzyl) phosphonate (**1**) to generate compound **2**, followed by alkylation with iodoalkanes to obtain various alkylated *tert*-butyl (4-((diethoxyphosphoryl)methyl)-phenyl)-carbamate (**3**−**5**). The obtained compounds **3**−**5** were coupled with corresponding aldehydes through the Horner−Wadsworth−Emmons reaction to generate *N*-alkylated *tert*-butyl (*E*)-(4-(4-(prop-2-yn-1-yloxy)styryl)phenyl)carbamate (**6**−**8**) having a propargyloxyl group in 72−74% yield, and *N*-alkylated *tert*-butyl (*E*)-(4-(4-((*tert*-butoxycarbonyl)(prop-2-yn-1-yl)-amino)styryl)phenyl)carbamate (**9**−**11**) with a Boc-protected propargylamino group in 68−72% yield. Click reactions between compounds **6**−**11** and 1-azido-2-fluoroethane catalyzed by copper(I) yielded fluorinated triazoles (**12**−**17**) in 50−60% yield, which underwent Boc-deprotection to give compounds **18**−**23** as the final products in 70−75% yield.

Fluorescence Properties. The excitation and emission spectra (0.3 mM in dichloromethane (DCM)) of the newly synthesized compounds were recorded using a Cary Eclipse fluorescent spectrophotometer. As shown in Figure 1, all compounds were fluorescent with excitation wavelengths in the range of 300−415 nm and emission wavelengths in the range of 394−600 nm.

In Vitro Staining of Intact Myelin. The newly synthesized compounds were first examined for myelin binding by in vitro staining of frozen mouse brain tissue sections. Because of the inherent fluorescence, the myelin-binding properties were directly examined by fluorescent microscopy after staining

DOI: 10.1021/acs.jmedchem.6b01328
J. Med. Chem. XXXX, XXX, XXX−XXX

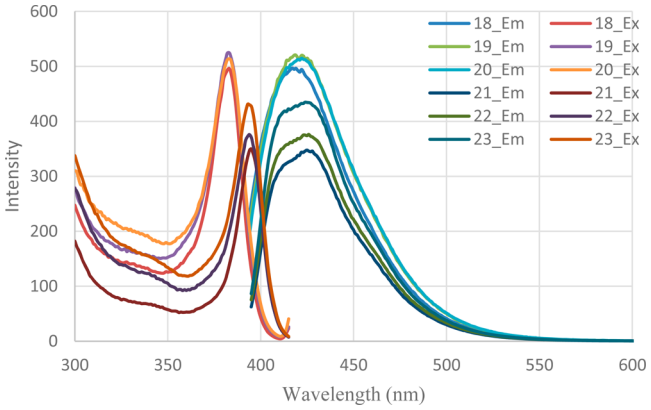

Figure 1. Excitation (Ex) and emission (Em) spectra of compounds **18**–**23** (0.3 mM in methylene chloride). Excitation spectra scans from 300 to 415 nm and emission spectra scans from 394 to 600 nm. Bandwidth at 5 nm, scan at 120 nm/min, and integration time of 0.5 s. Maximal excitation wavelengths of compounds **18**–**23** were at 375 and 395 nm, while maximal emission wavelengths of compounds **18**–**23** were at 430 nm.

with each tested compound at 10 μM concentration. All compounds labeled intact myelin sheaths present in the white matter included the corpus callosum, striatum, and cerebellum (Figure 2A,B). Because myelin is rich in white matter and deficient in gray matter, the difference of staining between the white matter and gray matter is expected to reflect binding specificity of the test compounds. We thus calculated the fluorescent intensity ratio (FIR) of each test compound in the same region of interest (ROI) between the white matter and gray matter using ImageJ.[12,19] As shown in Figure 2G, ROIs of same size were drawn on a representative region in the genu of the corpus callosum (gcc) and in the subcortical gray matter (cortex), respectively. The newly synthesized compounds fell into two categories based on the calculated FIR (Figure 2F). The three O-linked phenyl ring compounds (*E*)-4-(4-((1-(2-fluoroethyl)-1*H*-1,2,3-triazol-4-yl)methoxy)styryl)-*N*-alkane-aniline (**18**–**20**) showed FIRs ~ 1. The other three N-linked phenyl ring compounds (*E*)-*N*-((1-(2-fluoroethyl)-1*H*-1,2,3-triazol-4-yl)methyl)-4-(4-(alkane-amino)styryl)-aniline (**21**–**23**) showed FIRs ~ 1.5. The relatively higher FIRs indicated a higher degree of specific binding. This study suggests that an N-linked phenyl ring is more myelin-specific than an O-linked phenyl ring in terms of binding to myelin sheaths.

Lipophilicity. To penetrate the blood–brain barrier (BBB), lipophilicity is one of the three primary requirements that small molecules have to meet. Research showed that a lipophilicity value of 1.0–3.5 is ideal for a small molecule to cross the BBB.[24] On the basis of the structures, we calculated the

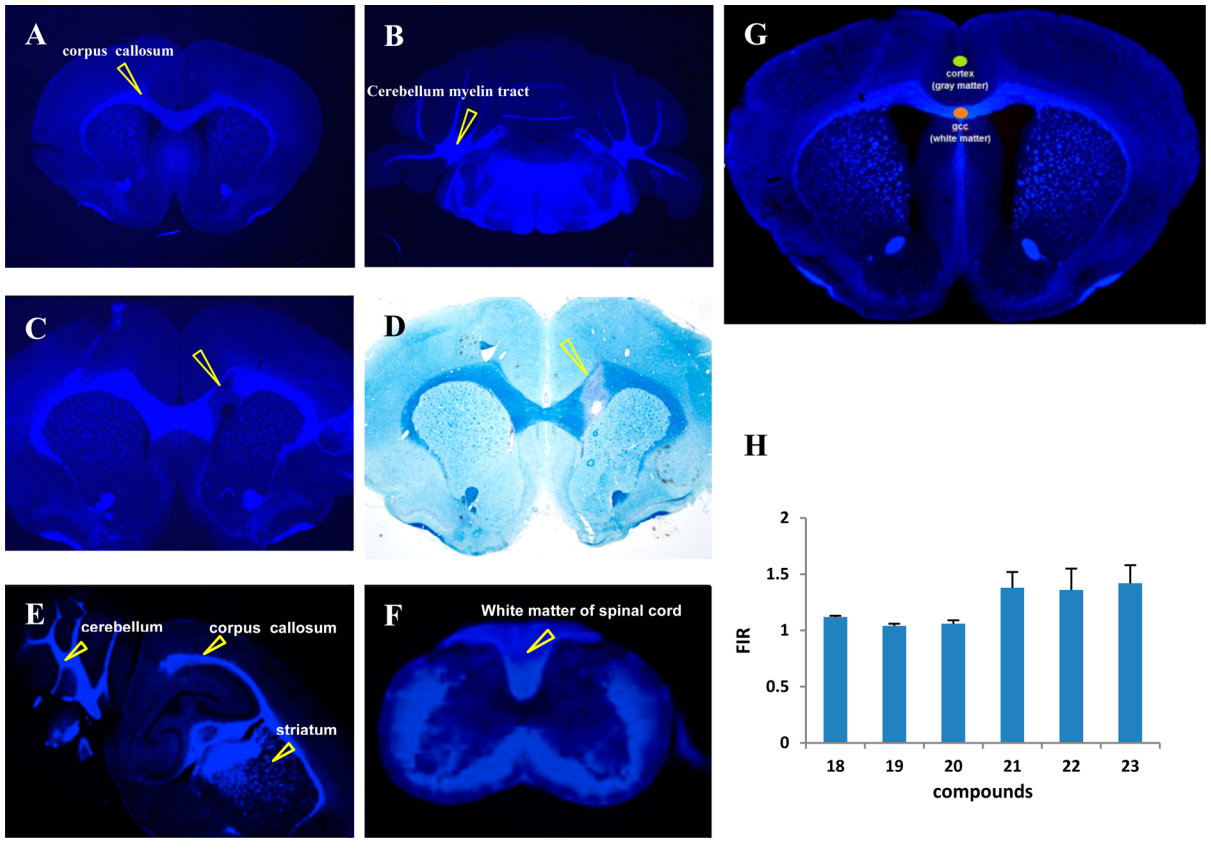

Figure 2. Tissue staining of compound **21** in wild-type mouse brain and demyelination LPC rat model brain, and preliminary compound screening with FIR calculated based on ROIs. Fresh frozen wild-type mouse brain sections were stained with compound **21**, and highly myelinated corpus callosum (A) and cerebellum myelin track (B) were clearly visualized. In vitro tissue staining showed that compound **21** can be used to detect demyelinated lesion present in a rat brain of LPC model (C), which is further confirmed by LFB and cresyl violet staining (D) on an adjacent tissue section. In situ staining proved that compound **21** crosses the BBB and stains myelinated areas of the mouse brain (E) and spinal cord (F). Representative in vitro tissue staining of coronal sections showing ROIs used for calculation of FIRs between white matter and gray matter (G), and FIRs of compounds **18**–**23** were calculated by ImageJ (H).

DOI: 10.1021/acs.jmedchem.6b01328
J. Med. Chem. XXXX, XXX, XXX–XXX

lipophilicity of the newly designed compounds as shown in Table 1. The ClogP value of N-linked compound **21** is 2.86, which is very similar to our model compound MeDAS (2.91). Thus, compound **21** was selected for further evaluation.

Table 1. Structures and ClogP of the Compounds Synthesized

Compound	Structure	Log P
18	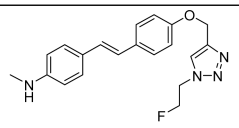	3.66
19	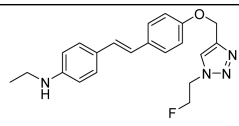	4.12
20	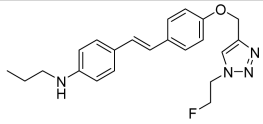	4.65
21	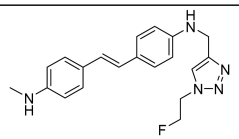	2.86
22	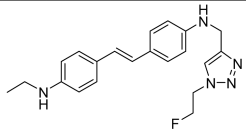	3.38
23	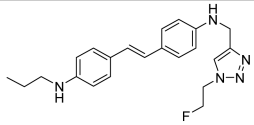	3.91

In Vitro Detection of Focal Demyelination in Rats. We then examined if compound **21** can be used to detect demyelinated lesions present in a rat model of focal demyelination. In this model, demyelination was induced by lysolecithin (LPC), which was stereotaxically injected into the corpus callosum of the right hemisphere. As shown in Figure 2C, compound **21** was capable of detecting the demyelinated focal lesion by fluorescent staining. The same foci of demyelination in the adjacent section were confirmed by conventional Luxol-Fast-Blue (LFB) and cresyl violet staining (Figure 2D). This result demonstrates that compound **21** can be used to detect brain lesions based on specific binding to myelin.

In Situ Staining of Compound 21. Following the in vitro studies, we then investigated the ability of compound **21** to readily enter the brain and bind to myelin in situ. A dose of 1.0 mg of compound **21** (50 mg/kg) was administered via the tail vein to wild-type (WT) mice. One hour after injection, the mice were perfused with saline followed by 4% paraformaldehyde (PFA) and the brain and spinal cord were removed and sectioned. The distribution of compound **21** was then directly examined under a fluorescent microscope. As shown in Figure 2E,F, strong fluorescence was visualized in the myelinated regions including the corpus callosum, striatum, cerebellar white matter, and the white matter of spinal cord. These studies suggest that compound **21** readily entered the brain and spinal cord and localized in all the myelinated regions in proportion to the myelin content.

Radiosynthesis. Encouraged by the in vitro and in situ results, we next evaluated the in vivo pharmacokinetic profiles of compound **21** after labeling with positron-emitting nuclide fluorine-18. As shown in Scheme 2, the radiosynthesis of [^{18}F]**21** was accomplished through a click reaction between compound **9** and 2-[^{18}F]fluoroethylazide ([^{18}F]**26**). [^{18}F]**26** was prepared through a nucleophilic substitution of tosylate compound **25** with [^{18}F]KF in the presence of K_2CO_3 and Kryptofix (K222) in MeCN at 95 °C for 10 min. The identity of the product was confirmed using analytical HPLC by coinjection with cold standard compound **21**. The radiochemical purity (RCP) of the final products was >98%, determined by analytical radio-HPLC. The specific activity at the end of synthesis was in the range of 1−2.5 Ci/μmol.

Quantitative MicroPET/CT Imaging Studies in WT Rats. Following radiosynthesis, the pharmacokinetic profile of [^{18}F]**21** was fully characterized by quantitative microPET/CT imaging in WT rats (n = 3). As shown in Figure 3, [^{18}F]**21** exhibited high uptake in the brain. The brain radioactivity peaked at 3 min postinjection followed by rapid clearance before reaching a plateau at 40−60 min postinjection. The time−radioactivity curve fitted well the equation $C_{(SUV)}$ = 1.1189 $e^{-0.0514t}$ + 0.3041, with a calculated time constant of clearance of 19.45 min.

In Situ Autoradiography. To validate the PET results and confirm that the PET signals were indeed from specific binding to myelin, we conducted ex vivo autoradiography in the mouse brain following administration of [^{18}F]**21** through tail vein injections. After 1 h, the mouse brain was dissected for coronal tissue sectioning. As shown in Figure 3E, [^{18}F]**21** distinctly labeled the corpus callosum, which is the region with a high density of myelin sheaths. The autoradiographic visualization showed that the distribution of [^{18}F]**21** was consistent with the histological staining of myelinated regions with the corresponding nonlabeled compound **21** (see Figure 2A). Thus, combination of in situ autoradiography and PET imaging confirmed that [^{18}F]**21** binds specifically to myelin in vivo.

Quantitative MicroPET/CT Imaging Studies in Shiverer Mice. To further evaluate the in vivo binding specificity of [^{18}F]**21**, we investigated the pharmacokinetic profiles of [^{18}F]**21** in a Shiverer mouse model that is deficient in myelin in the brain. Thus, the pharmacokinetic profiles of [^{18}F]**21** were quantitatively compared between Shiverer mice (C3Fe.SWV-Mbpshi/J, n = 2) and age-matched WT mice (CB57J, n = 2). During PET image acquisition, the Shiverer and WT mice were imaged side by side on the same bed for direct comparison.

DOI: 10.1021/acs.jmedchem.6b01328
J. Med. Chem. XXXX, XXX, XXX−XXX

Scheme 2. Radiosynthesis of [^{18}F]21 by Click Reaction Followed by Boc Deprotection

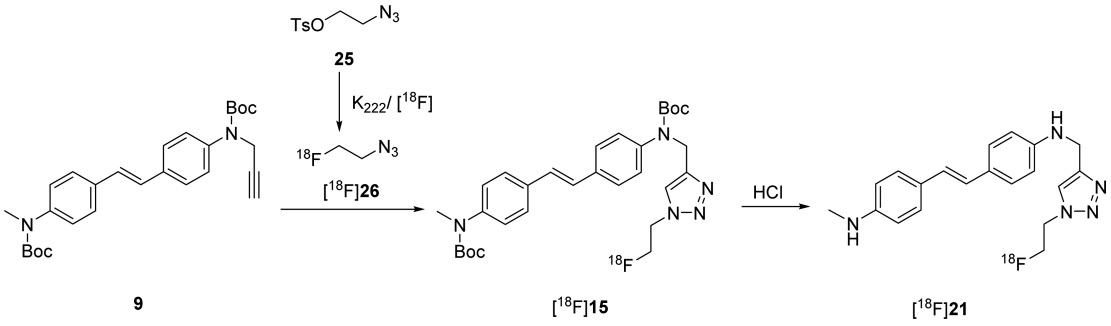

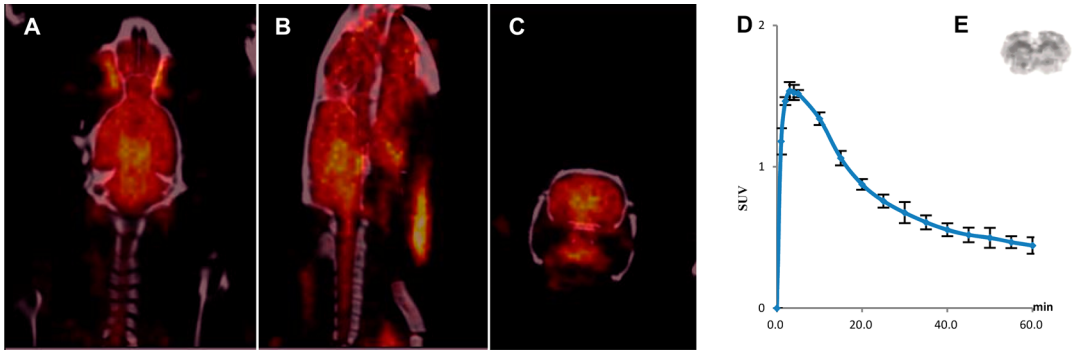

Figure 3. Representative (A) coronal, (B) sagittal, and (C) axial microPET/CT fusion images of the rat brain following iv administration of [^{18}F]**21**, showing high uptake in the white matter region of the brain. (D) Quantitative analysis of average radioactivity concentration of target compound [^{18}F]**21** in the whole brain of rats (n = 3) in terms of SUV as a function of time. (E) In situ autoradiography showing [^{18}F]**21** binds to myelinated corpus callosum in mouse brain (coronal) .

Dynamic emission scans were acquired for 60 min in 3D list mode immediately after [^{18}F]**21** (0.3 mCi each mouse, 11.1MBq) was administered. The brain uptake of [^{18}F]**21** was lower in the Shiverer brain than in the WT littermates (1.25 vs 1.64). After the brain concentration of [^{18}F]**21** reached a plateau, the SUVs from 40 to 60 min were summarized and compared. As shown in Figure 4, [^{18}F]**21** uptake in the Shiverer

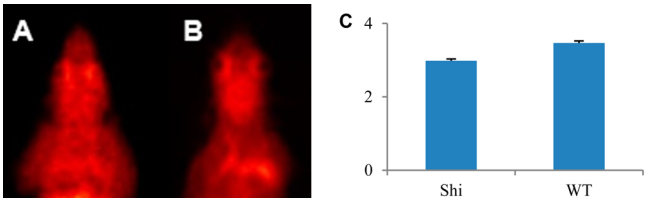

Figure 4. Representative coronal microPET images of the shiverer mouse brain (A) and WT mouse brain (B) following iv administration of [^{18}F]**21**, showing higher brain uptake in the control than that in the shiverer mouse. Quantitative analysis of total uptake of [^{18}F]**21** in terms of SUV at 40−60 min postinjection in shiverer mice [Shi] and control mouse [WT], showing significant higher uptake in WT mouse brain (p = 0.00028, two-tailed t test).

mouse brain was significantly decreased compared to the control mouse brain. These results suggested that [^{18}F]**21** indeed binds to myelin in the brain with high specificity.

Quantitative MicroPET/CT Imaging Studies in the Spinal Cord. So far, imaging of the spinal cord remains a great challenge. Our studies showed that compound **21** is capable of detecting focal demyelinated lesions induced in the rat brain in vitro. Next, we asked whether [^{18}F]**21** PET is capable of in vivo imaging of myelin deficiency or myelin damage in living animal models. We conducted [^{18}F]**21**-PET imaging in a rat model of thoracic contusive SCI. In this model, the contusion was made at T13 to introduce demyelination. In vivo [^{18}F]**21** PET imaging was performed before (as a baseline scan) and 1 day after contusion. The uptake of [^{18}F]**21** in every spine segment was then normalized to the average spine uptake. As shown in Figure 5A,B, the whole intact thoracic region of the spinal cord could be clearly visualized by [^{18}F]**21**-PET imaging in the control rats, but the lesion at vertebrae level T13 was clearly visualized by [^{18}F]**21**-PET in the SCI model (Figure 5C,D). Quantitative analysis of [^{18}F]**21** uptake in the whole thoracic region (T1-T13), and part of the lumbar vertebra showed distinct patterns of uptake. As shown in Figure 5E, the uptake of [^{18}F]**21** in T13 in the SCI group was 0.81, which was significantly lower than that in their own baseline scans (1.02). After microPET/CT imaging, we conducted in situ histological staining of the spinal cord 60 min after injection of nonlabeled compound **21** through the tail vein. As shown in Figure 6, in situ histological staining of the SCI (T13) tissue section with compound **21** showed that a demyelinated lesion was present at the dorsal column (A), which was confirmed by LFB and cresyl violet staining of the adjacent sections (B).

Coregistration of in Situ 3D Cryoimaging with MicroPET/CT Imaging. To confirm the in vivo imaging of the spinal white matter by PET/CT, we acquired 2D fluorescence images and generated a 3D reconstructed image stack. Thus, nonlabeled compound **21** was administered through tail vein injection into the rat after microPET/CT imaging of the spinal cord of SCI rats. One hour later, the rat was perfused with saline followed by 4% paraformaldehyde (PFA) and the spinal cord (T7-L2) was removed, sequentially sectioned, and imaged using a Leica fluorescent microscope.

DOI: 10.1021/acs.jmedchem.6b01328
J. Med. Chem. XXXX, XXX, XXX−XXX

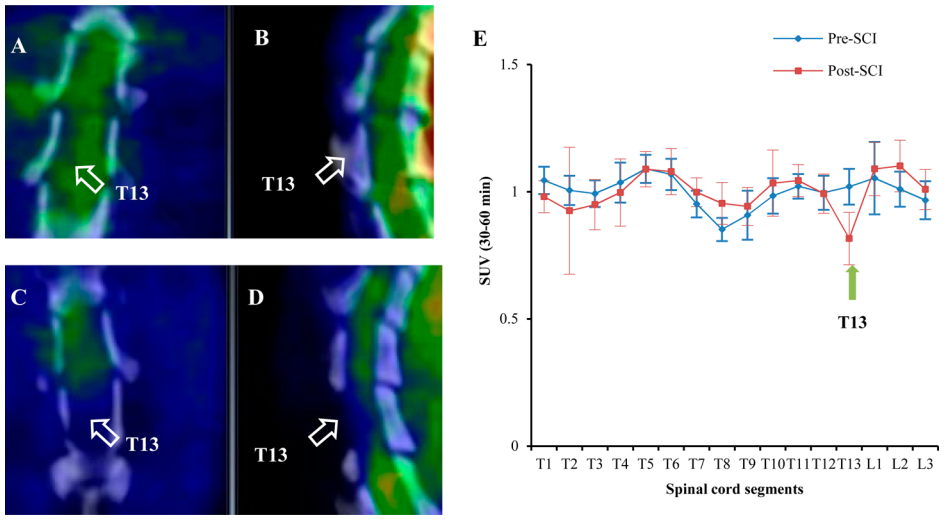

Figure 5. MicroPET/CT imaging. Representative PET/CT fusion images in rats acquired before SCI surgery (baseline scan) with higher magnification coronal (A) and sagittal images (B) in the T13 spinal cord. Representative PET/CT fusion images in rats acquired 1 day after SCI surgery with higher magnification coronal (C) and sagittal images (D) in the T13 spinal cord. Note the decrease signal contrast in the SCI animal compared with the baseline scan. (E) Quantification of the total cumulative [^{18}F]**21** uptake in the T13 ROI 30−60 post injection showed significantly lower uptake in the SCI group compared with baseline scans.

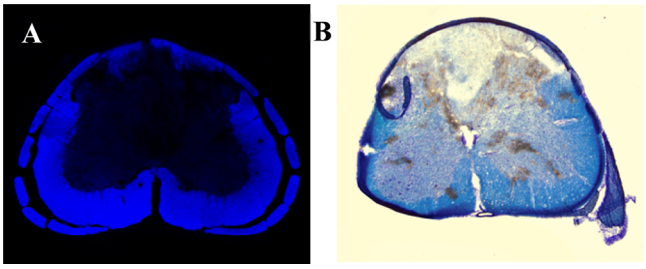

Figure 6. In situ histological staining of the SCI (T13) tissue section with reference compound **21** after microPET/CT imaging showing a demyelinated lesion at dorsal portion (A), which is consistent with LFB and cresyl violet staining using adjacent sections (B).

Slices were aligned sequentially using a semiautomated image registration algorithm through Matlab, giving a 3D reconstructed fluorescence image volume. Image volumes from fluorescence, PET, and CT were visualized in Amira using volume rendering and aligned based on the shape of the spine and fiducials from the vertebrae. As shown in Figure 7, 3D reconstructed fluorescence images (blue) were coregistered with microPET/CT images (yellow), where the reduced fluorescence signal was consistent with the reduced microPET signal in the same spinal cord region T13, thereby confirming that the reduced PET signal at the injury site was actually caused by demyelination after the T13 contusion.

DISCUSSION AND CONCLUSION

In this study, our goal was to developed a novel F-18-labeled radiotracer [^{18}F]**21** that can be used to quantitatively monitor myelin content in vivo. F-18-labeled radiotracers are often used to facilitate remote distribution of the tracer from a centralized radiopharmacy production site. On the basis of our previously developed C-11 myelin-imaging agent, MeDAS, we designed and synthesized a series of fluorinated analogues for SAR studies in order to identify lead candidates capable of in vivo imaging of myelin. In this work, we designed and synthesized a series of compounds by alkylating one of the terminal amino groups. Our previous studies suggested that the two terminal amino groups of MeDAS are essential moieties for specific binding to myelin. Alkylation of the amino groups does not adversely alter the binding properties, which makes it possible to introduce fluorine to the pharmacophore.

We first examined the lipophilicity of the newly synthesized compounds, which has a significant impact on brain permeability. Because introduction of fluorine to one amino group often renders the compound less lipophilic, we designed a series of fluorinated compounds by introducing an alkyl group into the other amino group to compensate for the decreased lipophilicity. The fluoro group was introduced through a Cu(I)-catalyzed Huisgen cycloaddition, known as the "click reaction", which can be conducted under mild conditions with high yield.[21,25−29] This striking versatility of Cu(I) catalyzed azide−alkyne cycloaddition has proven valuable in preparing PET radiopharmaceuticals.

After synthesis of compounds **18**−**23**, we conducted in vitro staining of mouse brain tissue sections. The binding specificity for myelin of each compound was estimated by calculating the FIR between the myelin-rich white matter and myelin-deficient gray matter.[17] As shown in Figure 1, these compounds had similar fluorescence properties (same excitation and emission wavelength), making it possible for direct comparison of myelin binding specificity based on the FIR when tissue staining was conducted using the same thickness of sections and the same exposure time of image acquisition. Our study suggested that N-linked analogues (**21**−**23**) exhibit higher myelin binding specificity than O-linked analogues (**18**−**20**). This may be in part due to the fact that introduction of O to the molecules renders the compounds more lipophilic as is evidenced by the higher LogP values shown in Table 1, which increase nonspecific binding.

Among those compounds with higher FIR, compound **21** was selected for further study as it has a logPoct value in the range between 1.5 and 3.5, which is often required for optimal brain uptake.[30] Combination of these studies led us to focus on compound **21** for further in situ staining, which is usually a practical way to determine brain permeability and in vivo

DOI: 10.1021/acs.jmedchem.6b01328
J. Med. Chem. XXXX, XXX, XXX−XXX

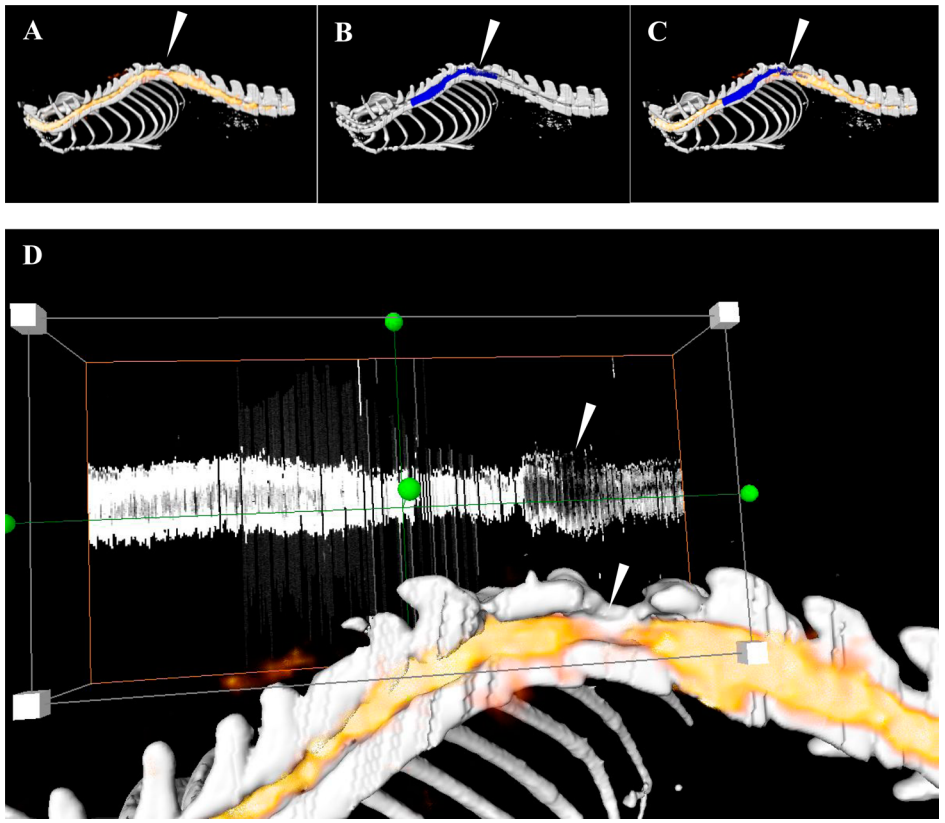

Figure 7. Coregistration of in situ 3D fluorescence imaging with microPET/CT imaging. (A) [^{18}F]**21** PET/CT imaging of spinal cord in SCI rat showing reduced uptake after contusive injury at T13 by the arrowhead. (B) 3D in situ fluorescence images of the spinal cord coregistered with CT image of the spinal cord in SCI rat showing reduced fluorescence intensity at T13 by the arrowhead. (C) Fusion images of PET, CT, and 3D fluorescence images. (D) Prior to 3D coregistration, a sagittal slice of the 3D fluorescence image stack indicates demyelination corresponding with microPET/CT imaging.

binding specificity of fluorescent compounds. Our studies indicate that compound **21** readily enters the brain and specifically binds to myelin in white matter regions such as the corpus callosum, striatum, and spinal cord. Furthermore, compound **21** is capable of detecting demyelinated lesions in a rat model of focal demyelination induced by LPC. These studies further confirmed that the characteristic brain uptake and staining of compound **21** is proportional to myelin content in the CNS.

Following in vitro and ex vivo studies, we proceeded with radiosynthesis of [^{18}F]**21** for in vivo PET imaging studies. The radiosynthesis was achieved by coupling 2-[^{18}F]fluoroethyl azide with its alkyne precursor compound **9** in the presence of excess Cu^{2+}/ascorbate and bathophenanthrolinedisulfonic acid disodium salt (BPDS) in aqueous solution, yielding the 1,2,3-triazoles product with the desired radiochemical yield (80–90%, n = 5, decay corrected) and radiochemical purity of over 98%. 2-[^{18}F]fluoroethyl azide is the key intermediate. Although the entire radiosynthesis could be conducted in a "one-pot" fashion, the radiochemical yield was relatively low. Separate isolation and purification of 2-[^{18}F]fluoroethyl azide was found to be critical for successful radiolabeling. Although [^{18}F]-fluoroethyl azide is highly volatile with a boiling point of 50 °C, distillation of [^{18}F]fluoroethyl azide from the reaction mixture was not practical. We thus used solid phase extraction (SPE) instead with two series of Waters Oasis HLB cartridges to successfully trap [^{18}F]fluoroethyl azide with high yield and purity.[31]

Following radiosynthesis, we conducted quantitative micro-PET/CT imaging studies in wild-type rats. An ideal radiotracer for in vivo PET imaging of myelin should meet several criteria such as high brain uptake and prolonged retention due to high myelin-binding potential. As expected, quantitative PET data analysis showed a high and rapid accumulation of [^{18}F]**21** in the brain followed by a rapid nonspecific binding clearance. In situ autoradiography further confirmed that the radioactivity signal detected by PET indeed reflects the specific spatial distribution of [^{18}F]**21** after binding to myelinated fibers. The combination of in situ autoradiography with [^{18}F]**21** and with PET imaging studies confirmed that [^{18}F]**21** is a specific imaging marker of myelin content.

Given the fact that [^{18}F]**21** binds to myelin sheaths in vivo, we further determined whether [^{18}F]**21**-PET is capable of imaging myelin deficiency or damage as tested in two animal models. The Shiverer mouse model was used to represent a myelin-deficiency in the brain, while the rat model with traumatic SCI was used to represent myelin damage in the spinal cord. As shown in Figure 5, quantitative analysis of the uptake of [^{18}F]**21** in the brain showed that retention in the Shiverer mice was significantly lower than that in the WT control (p = 0.00028, two-tailed t test). MicroPET/CT imaging in the SCI rat model further confirmed that [^{18}F]**21** is capable of detecting and quantifying myelin damage in the spinal cord. As shown in Figure 6, a distinct myelin-imaging defect at T13 contused tissue could be visualized and quantified directly by PET/CT imaging. Before contusion, [^{18}F]**21** uptakes at T12, T13, and L1 spine segments were respectively 0.99, 1.02, and

DOI: 10.1021/acs.jmedchem.6b01328
J. Med. Chem. XXXX, XXX, XXX−XXX

1.05, while the uptakes were 0.99, 0.81, and 1.08 1 day post-T13 contusion. [^{18}F]**21** uptake decreased dramatically at the site of injury (T13) compared with its own baseline scan.

To date, to expedite the translation of myelin imaging into clinical practice, some radiotracers such as PIB and florbetaben that were originally developed for amyloid imaging have been repurposed for myelin imaging.[32,33] These radiotracers have already been approved by the FDA for clinical use. Such radiotracers were found to bind to the myelin-rich white matter in the brain, albeit to a lesser extent than amyloid deposits. It is thus believed that they could directly be used in MS patients to image myelin distribution in the white matter region where no amyloid deposits would be present, even in Alzheimer's patients. Thus, the utility of these amyloid-imaging radiotracers were tested in various subtypes of MS patients for correlation of tracer uptake with MRI characterization of brain lesions, disease progression patterns, and functional disability. These studies provided proof-of-the-concept that PET imaging is a valid clinical imaging tool to observe white matter changes in terms of myelin distribution. However, these radiotracers originally were so optimized for amyloid imaging that any binding potential in the white matter was minimized. This makes it difficult to address several important issues concerning imaging sensitivity and specificity under an inflammatory condition that is typical of MS. Independent studies often led to controversial interpretations of imaging results.

To overcome these limitations and enhance the myelin-imaging sensitivity and specificity, new myelin-imaging radiotracers must be developed whereby the binding potential for myelin can be maximized in the white matter. The parent compound, MeDAS, was thus optimized to be specific for myelin and to minimize any effect of inflammation. On the basis of solid preclinical validation, it will significantly improve the imaging sensitivity and specificity.

An important innovative aspect of this work lies in the combination of PET/CT with 3D cryoimaging. PET is a tomographic, functional imaging modality with high quantitative capacity. Yet, PET quantitative analysis must be validated by correlation with histological characterization. This is often a very challenging task, particularly in spinal cord imaging due to its small and mobile structure. Tissue preparation and sectioning are very time-consuming, and only selected tissue sections can be used for validation of PET-imaging results, which is likely biased by the limited scope of sampling. Tomographic cryoimaging thus can overcome this limitation as it can provide high-resolution, three-dimensional images of the entire spinal cord for histological characterization. The whole process can be fully automated using a CryoViz system (BioInVision, Inc.).[34,35] The imaging results are thus less subjective as the sampling bias can be essentially eliminated. More importantly, the 3D cryoimaging of the spinal cord was carried out in situ using nonlabeled, otherwise identical compound **21**, which was administered via tail vein injection in a way similar to the PET scan. This promotes accurate image coregistration between PET and cryoimaging for quantitative analysis.

This new multimodality PET/cryoimaging technique was first applied in the studies of SCI. In vivo imaging of myelin changes after SCI is of particular importance as demyelination and remyelination have direct effects on disability and functional recovery. To confirm that the contusive injury at T13 was associated directly with demyelination rather than tissue loss, we conducted in situ 3D cryoimaging with fluorescent compound **21** following microPET/CT imaging using [^{18}F]**21**. As shown in Figure 6A, a distinct demyelination at the dorsal portion was observed. This was further confirmed by standard LFB and cresyl violet staining of myelin sheaths on the adjacent sections, which suggests there was a significant demyelinated lesion in the white matter region at the injury site. In contrast, no tissue loss was observed and myelinated white matter outside the injured region remained intact (Figure 7B). After tomographic 3D reconstruction, the cryoimages were coregistered with PET/CT images (Figure 7). We observed a significant reduction of the fluorescence signal in the lesion region of the spinal cord, validating the sensitivity and specificity of PET. These findings suggest that [^{18}F]**21**-PET imaging can be used as a diagnostic marker of myelin damage. In addition, we demonstrated, for the first time, the feasibility of simultaneous coregistration of PET/CT with and validation by high-resolution, 3D cryoimaging, which allows for seamless combination of physiological information with the high sensitivity and quantification capability provided by PET and microscopic histology provided by cryoimaging. This newly developed multimodality imaging technique should greatly facilitate radiotracer development and efficacy evaluation of novel therapies.

In summary, a series of fluorinated fluorescent myelin-binding agents was synthesized for PET and 3D cryoimaging. Following systematic SAR studies, we identified a novel myelin-imaging agent (TAFDAS, **21**) that readily penetrates the BBB and binds to myelin membranes in the brain and spinal cord. Sequential [^{18}F]**21**-PET imaging and 3D cryoimaging in a contusion rat model of SCI demonstrate, for the first time, that combination of PET and cryoimaging is a new imaging tool with high sensitivity, specificity, and spatial resolution.

EXPERIMENTAL SECTION

Methods and Materials. Chemicals and reagents were used as received without further purification. Glassware was dried in an oven at 130 °C and purged with a dry atmosphere prior to use. Unless otherwise mentioned, reactions were performed open to air. Reactions were monitored by TLC and visualized by a dual short/long wave UV lamp. Column flash chromatography was performed using 230−400 mesh silica gel (Fisher). Preparative TLC was performed on Analtech Preparative TLC Uniplates with UV254 fluorescence indicator (500 μm). NMR spectra were recorded on a Varian Inova 400 spectrometer and 500 MHz Bruker Ascend Avance III HD at room temperature. Florescence spectra were recorded, and chemical shifts for ^{1}H and ^{13}C NMR were reported as δ, part per million (ppm), and referenced to an internal deuterated solvent central line. The abbreviations s, br s, d, dd, ddd, br d, t, dt, q, m, and br m stand for their resonance multiplicity singlet, broad singlet, doublet, doublet of doublets, doublet of doublet of doublets, broad doublets, triplet, triplets of doublets, quartet, multiplet, and broad multiplet, respectively, which were calculated automatically on a MestReNova 10.0. The purity of tested compounds as determined by analytical HPLC was 95%. HRMS-ESI mass spectra were acquired on an Agilent Q-TOF. UV absorption was measured on a Cary 50 Bio spectrophotometer using a standard 1 cm × 1 cm quartz cuvette. Fluorescence was measured with a Cary Eclipse spectrophotometer using a 1 cm × 1 cm quartz cuvette.

*General Method for Alkylation of tert-Butyl (4-((Diethoxyphosphoryl)methyl)phenyl)carbamate (**3**−**5**).* To an oven-dried 100 mL round-bottom flask purged with argon gas and fitted with a magnetic stir bar, sodium hydride (2 equiv 95%) and *tert*-butyl (4-((diethoxyphosphoryl) methyl)phenyl)carbamate (1 equiv) were added together with dry THF (25 mL) at 0 °C and purged with argon gas. Iodo-alkane (3 equiv) was added slowly dropwise after 30 min at 0 °C under argon gas. The reaction was stirred under argon and allowed to reach room temperature overnight. After completion, the

DOI: 10.1021/acs.jmedchem.6b01328
J. Med. Chem. XXXX, XXX, XXX−XXX

reaction was quenched with water and THF was removed in vacuum. The residue was dissolved in DCM and water and the aqueous layer was extracted three times with DCM (30 mL). The organic layers were combined and washed twice with water (50 mL) and once with brine (50 mL). The organic layer was dried over Na_2SO_4 and concentrated to give the desired product as a sticky oil, which was used for the next step without further purification.

*General Method for Horner–Wadsworth–Emmons Coupling Reaction (**6**–**11**).* To an oven-dried 100 mL round-bottom flask with a magnetic stir bar was added sodium hydride (2 equiv, 95%). The flask was purged with argon, and 2 mL of dry DMF was added. This solution was cooled to 0 °C, and the phosphonate in DMF (2 mL) was added. The mixture was allowed to stir for 1 h at 0 °C. Then the aldehyde in 2 mL of DMF was added slowly. The reaction was continued for another 2 h at 0 °C under argon followed by quenching with water (50 mL) and then extracted with ethyl acetate (50 mL) three times. The organic layer was washed with saturated $NaHCO_3$ (20 mL) and brine (50 mL), dried with Na_2SO_4, and concentrated to give the crude product, which was purified with flash chromatography using hexanes and ethyl acetate as eluents.

*tert-Butyl (E)-Ethyl(4-(4-(prop-2-yn-1-yloxy)styryl)phenyl)-carbamate (**7**).* ^{1}H NMR (400 MHz, chloroform-*d*) δ 7.43–7.36 (m, 4H), 7.13 (d, *J* = 8.2 Hz, 2H), 6.98 (d, *J* = 16.3 Hz, 1H), 6.93 (d, *J* = 1.9 Hz, 2H), 6.90 (d, *J* = 7.4 Hz, 1H), 4.63 (dd, *J* = 2.5, 1.1 Hz, 2H), 3.65 (q, *J* = 7.1 Hz, 2H), 2.50 (t, *J* = 2.4 Hz, 1H), 1.42 (s, 9H), 1.13 (t, *J* = 7.1 Hz, 3H). ^{13}C NMR (100 MHz, chloroform-*d*) δ 157.4, 154.6, 141.7, 135.3, 131.1, 128.1, 127.9, 127.2, 126.7, 126.5, 115.3, 80.2, 78.7, 76.0, 56.0, 45.1, 28.6, 14.2.

*tert-Butyl (E)-Propyl(4-(4-(prop-2-yn-1-yloxy)styryl)phenyl)-carbamate (**8**).* ^{1}H NMR (400 MHz, chloroform-*d*) δ 7.40 (dd, *J* = 8.7, 2.1 Hz, 4H), 7.14 (d, *J* = 8.1 Hz, 2H), 6.99 (d, *J* = 16.5 Hz, 1H), 6.93 (s, 2H), 6.90 (d, *J* = 7.1 Hz, 1H), 4.63 (d, *J* = 2.4 Hz, 2H), 3.62–3.54 (m, 2H), 2.50 (s, 1H), 1.61–1.49 (m, 2H), 1.43 (s, 9H), 0.87 (t, *J* = 7.4 Hz, 3H). ^{13}C NMR (100 MHz, chloroform-*d*) δ 157.4, 154.9, 141.8, 135.3, 131.1, 128.2, 127.9, 127.3, 126.7, 126.5, 115.3, 80.2, 78.7, 76.0, 55.99, 51.8, 28.6, 22.0, 11.4.

*tert-Butyl (E)-(4-(4-((tert-Butoxycarbonyl)(prop-2-yn-1-yl)amino)-styryl)phenyl)(methyl)carbamate (**9**).* ^{1}H NMR (400 MHz, chloroform-*d*) δ 7.46 (dd, *J* = 8.7, 6.7 Hz, 4H), 7.31 (d, *J* = 8.2 Hz, 2H), 7.22 (d, *J* = 8.6 Hz, 2H), 7.03 (s, 2H), 4.37 (d, *J* = 2.5 Hz, 2H), 3.26 (s, 3H), 2.27–2.24 (t, *J* = 4.8 1H), 1.46 (s, 18H). ^{13}C NMR (100 MHz, chloroform-*d*) δ 154.8, 154.1, 143.3, 141.5, 135.4, 134.4, 128.2, 127.9, 127.8, 126.9, 126.8, 126.5, 125.6, 81.4, 80.6, 80.2, 72.1, 39.9, 37.4, 28.5, 28.5.

*tert-Butyl (E)-(4-(4-((tert-Butoxycarbonyl)(prop-2-yn-1-yl)amino)-styryl)phenyl)(ethyl)carbamate (**10**).* ^{1}H NMR (400 MHz, chloroform-*d*) δ 7.45–7.42 (m, 4H), 7.28 (d, *J* = 8.4 Hz, 2H), 7.14 (d, *J* = 8.5 Hz, 2H), 7.01 (s, 2H), 4.32 (d, *J* = 2.4 Hz, 2H), 3.65 (q, *J* = 7.0 Hz, 2H), 2.23 (t, *J* = 2.4 Hz, 1H), 1.44 (s, 9H), 1.44 (s, 9H), 1.12 (t, *J* = 7.1 Hz, 3H). ^{13}C NMR (100 MHz, chloroform-*d*) δ 154.6, 154.1, 142.0, 141.6, 135.4, 135.0, 128.3, 128.0, 127.2, 126.9, 126.9, 126.5, 81.4, 80.3, 80.2, 72.1, 45.0, 39.9, 28.6, 28.5, 14.1.

*tert-Butyl (E)-(4-(4-((tert-Butoxycarbonyl)(prop-2-yn-1-yl)amino)-styryl)phenyl)(propyl)carbamate (**11**).* ^{1}H NMR (400 MHz, chloroform-*d*) δ 7.48–7.45 (m, 4H), 7.31 (d, *J* = 8.4 Hz, 2H), 7.18 (d, *J* = 8.3 Hz, 2H), 7.05 (s, 2H), 4.37 (d, *J* = 2.5 Hz, 2H), 3.62–3.58 (m, 2H), 2.26 (t, *J* = 2.4 Hz, 1H), 1.63–1.52 (m, 2H), 1.47 (s, 9H), 1.44 (s, 9H), 0.89 (t, *J* = 7.4 Hz, 3H). ^{13}C NMR (100 MHz, chloroform-*d*) δ 154.9, 154.1, 142.2, 141.6, 135.4, 135.0, 128.3, 128.0, 127.3, 126.9, 126.5, 81.4, 80.2, 80.2, 72.0, 51.7, 39.9, 28.5, 28.4, 21.9, 11.4.

General Method for Click Chemistry (12–17). A portion of 1-(4-methylbenzenesulfonate)-2-fluoroethanol (1.67 equiv) in DMF (4 mL) was stirred with a suspension of sodium azide (5.6 equiv) at room temperature. After 48 h, the solution was filtered through Celite and the crude 1-azido-2-fluoroethane was used immediately in the next step without further purification. In a separate flask, copper(I) iodide (5.4 equiv) was suspended in methanol (2 mL) under an argon atmosphere with vigorous stirring. In rapid succession, the alkyne precursor (1 equiv) dissolved in methanol (1 mL), the crude 1-azido-2-fluoroethane dissolved in DMF, and triethylamine (5.4 equiv) were added. The reaction mixture was stirred overnight at room temperature, and saturated $NaHCO_3$ (20 mL) was then added followed by extraction with ethyl acetate (20 mL) three times. The combined organic layers were washed with water (50 mL) and brine (50 mL), dried with Na_2SO_4, and concentrated to give the crude product, which was purified by column chromatography eluted with hexanes and ethyl acetate.

*tert-Butyl (E)-(4-(4-((1-(2-Fluoroethyl)-1H-1,2,3-triazol-4-yl)-methoxy)styryl)phenyl)(methyl)carbamate (**12**).* ^{1}H NMR (400 MHz, chloroform-*d*) δ 7.70 (d, *J* = 1.0 Hz, 1H), 7.40 (dd, *J* = 8.7, 3.0 Hz, 4H), 7.17 (d, *J* = 8.5 Hz, 2H), 6.95 (s, 3H), 6.93 (d, *J* = 22.8 Hz, 4H), 6.90 (d, *J* = 16.5 Hz, 2H), 4.81 (dd, *J* = 5.2, 4.1 Hz, 1H), 4.67 (ddd, *J* = 14.2, 5.5, 4.3 Hz, 2H), 4.59 (dd, *J* = 5.2, 3.9 Hz, 1H), 3.22 (s, 3H), 1.42 (s, 9H). ^{13}C NMR (100 MHz, chloroform-*d*) δ 158.0, 154.9, 144.6, 143.0, 134.7, 130.8, 128.0, 127.9, 126.5, 126.4, 125.7, 124.0, 115.2, 114.8, 82.5, 80.8, 80.6, 62.1, 50.9, 50.7, 37.4, 28.5.

*tert-Butyl (E)-(4-(4-((1-(2-Fluoroethyl)-1H-1,2,3-triazol-4yl)-methoxy)styryl)phenyl)(ethyl)carbamate (**13**).* ^{1}H NMR (400 MHz, chloroform-*d*) δ 7.72–7.70 (m, 1H), 7.40 (dd, *J* = 8.6, 1.8 Hz, 4H), 7.12 (d, *J* = 8.1 Hz, 2H), 6.98 (d, *J* = 16.3 Hz, 1H), 6.96–6.93 (m, 2H), 6.91 (d, *J* = 15.9 Hz, 1H), 5.19 (s, 2H), 4.81 (dd, *J* = 5.2, 4.1 Hz, 1H), 4.75–4.65 (m, 2H), 4.59 (dd, *J* = 5.2, 4.0 Hz, 1H), 3.64 (q, *J* = 7.1 Hz, 2H), 1.40 (s, 9H), 1.12 (t, *J* = 7.1 Hz, 3H). ^{13}C NMR (100 MHz, chloroform-*d*) δ 158.0, 154.7, 144.6, 141.7, 135.3, 130.8, 128.1, 127.9, 127.2, 126.7, 126.4, 124.0, 115.2, 114.8, 82.5, 80.8, 80.2, 62.1, 50.9, 50.7, 45.1, 28.6, 14.1.

*tert-Butyl (E)-(4-(4-((1-(2-Fluoroethyl)-1H-1,2,3-triazol-4-yl)-methoxy)styryl)phenyl)(propyl)carbamate (**14**).* ^{1}H NMR (400 MHz, chloroform-*d*) δ 7.70 (s, 1H), 7.40 (dd, *J* = 8.7, 1.9 Hz, 4H), 7.12 (d, *J* = 8.1 Hz, 2H), 6.98 (d, *J* = 16.2 Hz, 1H), 6.96–6.93 (m, 2H), 6.91 (d, *J* = 16.2 Hz, 1H), 5.18 (s, 2H), 4.80 (dd, *J* = 5.2, 4.1 Hz, 1H), 4.67 (ddd, *J* = 14.2, 5.4, 4.3 Hz, 2H), 4.58 (dd, *J* = 5.2, 4.0 Hz, 1H), 3.59–3.52 (m, 2H), 1.57–1.47 (m, 2H), 1.40 (s, 9H), 0.84 (t, *J* = 7.4 Hz, 3H). ^{13}C NMR (100 MHz, chloroform-*d*) δ 158.1, 154.9, 144.7, 141.8, 135.3, 130.9, 128.1, 127.9, 127.3, 126.7, 126.4, 124.0, 115.2, 114.8, 82.5, 80.8, 80.2, 62.2, 51.7, 50.9, 50.7, 28.5, 21.9, 11.4.

*tert-Butyl (E)-(4-(4-((tert-Butoxycarbonyl)((1-(2-fluoroethyl)-1H-1,2,3-triazol-4-yl)methyl)amino)-styryl)phenyl)(methyl)carbamate (**15**).* ^{1}H NMR (400 MHz, chloroform-*d*) δ 7.68 (s, 1H), 7.44 (dd, *J* = 8.7, 6.9 Hz, 4H), 7.28 (d, *J* = 7.8 Hz, 2H), 7.22 (d, *J* = 8.6 Hz, 2H), 7.02 (s, 2H), 4.92 (s, 2H), 4.84 (dd, *J* = 5.2, 4.1 Hz, 1H), 4.71 (ddd, *J* = 13.2, 5.3, 4.3 Hz, 2H), 4.62 (dd, *J* = 5.1, 4.1 Hz, 1H), 3.27 (s, 3H), 1.46 (s, 9H), 1.45 (s, 9H). ^{13}C NMR (100 MHz, chloroform-*d*) δ 154.6, 154.5, 145.9, 143.3, 142.1, 135.0, 134.5, 128.1, 127.9, 126.8, 126.7, 126.4, 125.6, 123.9, 82.6, 81.2, 80.9, 80.6, 50.8, 50.6, 46.0, 37.4, 28.5, 28.5.

*tert-Butyl (E)-(4-(4-((tert-Butoxycarbonyl)((1-(2-fluoroethyl)-1H-1,2,3-triazol-4-yl)methyl)amino)-styryl)phenyl)(ethyl)carbamate (**16**).* ^{1}H NMR (400 MHz, chloroform-*d*) δ 7.73–7.62 (m, 1H), 7.45 (t, *J* = 8.5 Hz, 4H), 7.31–7.26 (m, 2H), 7.17 (d, *J* = 8.5 Hz, 2H), 7.03 (s, 2H), 4.92 (s, 2H), 4.82 (dd, *J* = 5.2, 4.1 Hz, 1H), 4.69 (ddd, *J* = 12.4, 5.5, 4.3 Hz, 2H), 4.61 (dd, *J* = 5.2, 4.0 Hz, 1H), 3.68 (q, *J* = 7.1 Hz, 2H), 1.45 (s, 9H), 1.44 (s, 9H), 1.16 (t, *J* = 7.1 Hz, 3H). ^{13}C NMR (100 MHz, chloroform-*d*) δ 154.6, 154.45, 145.9, 142.1, 141.95, 135.0, 128.1, 128.0, 127.2, 126.9, 126.8, 126.4, 123.9, 82.6, 81.2, 80.9, 80.3, 50.8, 50.6, 46.0, 45.0, 28.5, 28.5, 14.1.

*tert-Butyl (E)-(4-(4-((tert-Butoxycarbonyl)((1-(2-fluoroethyl)-1H-1,2,3-triazol-4-yl)methyl)amino)-styryl)phenyl)(propyl)carbamate (**17**).* ^{1}H NMR (400 MHz, chloroform-*d*) δ 7.68 (s, 1H), 7.45 (dd, *J* = 9.0, 7.2 Hz, 4H), 7.28 (d, *J* = 9.0 Hz, 2H), 7.17 (d, *J* = 8.4 Hz, 2H), 7.03 (s, 2H), 4.92 (s, 2H), 4.84 (dd, *J* = 5.2, 4.1 Hz, 1H), 4.71 (ddd, *J* = 13.2, 5.5, 4.3 Hz, 2H), 4.63 (dd, *J* = 5.2, 4.0 Hz, 1H), 1.62–1.53 (m, 2H), 1.45 (s, 9H), 1.44 (s, 9H), 0.89 (t, *J* = 7.4 Hz, 3H), 0.89 (t, *J* = 12.0 Hz, 3H). ^{13}C NMR (100 MHz, $CDCl_3$) δ 154.9, 154.5, 146.0, 142.1, 135.0, 128.1, 128.0, 127.3, 126.9, 126.4, 123.9, 82.6, 81.2, 80.9, 80.26, 51.7, 50.8, 50.6, 46.0, 28.5, 28.5, 21.9, 11.4.

General Method for Boc Deprotection (18–23). The click product was dissolved in 2 mL of methanol. To this mixture was added 2 mL of HCl (1.2 M), and the mixture was stirred for 1.5 h at 60 °C and then sufficient NaOH (1 M) was added to bring the pH to 10. Water was added to the mixture and extracted with ethyl acetate (10

DOI: 10.1021/acs.jmedchem.6b01328
J. Med. Chem. XXXX, XXX, XXX–XXX

mL) three times, washed with brine (30 mL), dried with Na_2SO_4, and concentrated to give the crude product. Prep TLC or flash chromatography (hexanes/acetone) yielded the deprotected product.

*(E)-4-(4-((1-(2-Fluoroethyl)-1H-1,2,3-triazol-4-yl)methoxy)styryl)-N-methylaniline (**18**).* ^{1}H NMR (400 MHz, DMSO-d_6) δ 8.27 (s, 1H), 7.44 (d, J = 8.8 Hz, 2H), 7.31 (d, J = 8.6 Hz, 2H), 7.07−6.98 (m, 2H), 6.94 (d, J = 16.4 Hz, 1H), 6.85 (d, J = 16.4 Hz, 1H), 6.52 (d, J = 8.7 Hz, 2H), 5.82 (q, J = 5.0 Hz, 1H), 5.16 (s, 2H), 4.89 (dd, J = 5.3, 4.1 Hz, 1H), 4.81−4.75 (m, 2H), 4.73−4.67 (m, 1H), 2.69 (d, J = 5.1 Hz, 3H). ^{13}C NMR (125 MHz, DMSO-d_6) δ 157.4, 149.9, 143.4, 131.5, 127.8, 127.5, 127.4, 125.4, 125.3, 122.9, 115.3, 112.1, 83.0, 81.7, 61.5, 50.6, 50.4, 30.1. HR-MS (ESI) m/z calculated for ($C_{20}H_{22}FN_4O$) $[M + H]^+$ 353.1772, found 353.1773. HPLC purity: 96.94%, retention time 4.00 min. C-18 reversed-phase HPLC (Phenomenex, 10 mm × 250 mm); eluent, acetonitrile:H_2O = 40:60; flow rate of 1.0 mL/min.

*(E)-4-(4-((1-(2-Fluoroethyl)-1H-1,2,3-triazol-4-yl)methoxy)styryl)-N-ethylaniline (**19**).* ^{1}H NMR (500 MHz, chloroform-d) δ 7.74 (s, 1H), 7.40 (d, J = 8.1 Hz, 2H), 7.33 (d, J = 8.0 Hz, 2H), 6.96 (d, J = 8.1 Hz, 2H), 6.90 (d, J = 16.3 Hz, 1H), 6.84 (d, J = 16.3 Hz, 1H), 6.59 (d, J = 8.0 Hz, 2H), 5.24 (s, 2H), 4.85 (t, J = 4.8 Hz, 1H), 4.76 (t, J = 4.8 Hz, 1H), 4.71 (t, J = 4.8 Hz, 1H), 4.65 (t, J = 4.8 Hz, 1H), 3.18 (q, J = 7.1 Hz, 2H), 1.27 (t, J = 6.7 Hz, 3H). ^{13}C NMR (125 MHz, chloroform-d) δ 157.2, 147.8, 144.7, 131.6, 127.5, 127.3, 127.2, 126.9, 123.8, 123.7, 115.0, 112.8, 82.2, 80.8, 62.0, 50.7, 50.5, 38.5, 14.8. HR-MS (ESI) m/z calculated for ($C_{21}H_{24}FN_4O$) $[M + H]^+$ 367.1929, found 367.1932. HPLC purity: 96.22%, retention time 4.02 min. C-18 reversed-phase HPLC (Phenomenex, 10 mm × 250 mm); eluent, acetonitrile:H_2O = 40:60; flow rate of 1.0 mL/min.

*(E)-4-(4-((1-(2-Fluoroethyl)-1H-1,2,3-triazol-4-yl)methoxy)styryl)-N-propylaniline (**20**).* ^{1}H NMR (400 MHz, chloroform-d) δ 7.68 (s, 1H), 7.33 (d, J = 8.7 Hz, 2H), 7.25 (d, J = 8.5 Hz, 2H), 6.89 (d, J = 8.7 Hz, 2H), 6.83 (d, J = 16.2 Hz, 1H), 6.77 (d, J = 16.3 Hz, 1H), 6.51 (d, J = 8.5 Hz, 2H), 5.17 (s, 2H), 4.80 (dd, J = 5.2, 4.1 Hz, 1H), 4.67 (dt, J = 13.4, 4.6 Hz, 2H), 4.61−4.56 (m, 1H), 3.04 (t, J = 7.1 Hz, 2H), 1.57 (p, J = 7.3 Hz, 2H), 0.93 (t, J = 7.4 Hz, 3H). ^{13}C NMR (100 MHz, chloroform-d) δ 157.4, 148.2, 144.9, 131.8, 127.7, 127.4, 127.3, 126.9, 123.9, 115.1, 112.9, 82.5, 80.8, 62.2, 50.9, 50.7, 45.9, 22.9, 11.8. HR-MS (ESI) m/z calculated for ($C_{22}H_{26}FN_4O$) $[M + H]^+$ 381.2085, found 381.2090. HPLC purity: 96.28%, retention time 6.50 min. C-18 reversed-phase HPLC (Phenomenex, 10 mm × 250 mm); eluent, acetonitrile:H_2O = 40:60; flow rate of 1.0 mL/min.

*(E)-N-((1-(2-Fluoroethyl)-1H-1,2,3-triazol-4-yl)methyl)-4-(4-(methylamino)styryl)aniline (**21**).* ^{1}H NMR (400 MHz, chloroform-d) δ 7.55 (s, 1H), 7.32 (dd, J = 8.6, 1.8 Hz, 4H), 6.83 (d, J = 1.7 Hz, 2H), 6.64 (d, J = 8.6 Hz, 2H), 6.58 (d, J = 8.6 Hz, 2H), 4.82 (dd, J = 5.1, 4.2 Hz, 1H), 4.71 (dd, J = 5.2, 4.1 Hz, 1H), 4.65 (dd, J = 5.2, 4.2 Hz, 1H), 4.59 (dd, J = 5.2, 4.1 Hz, 1H), 2.85 (s, 3H). ^{13}C NMR (100 MHz, chloroform-d) δ 148.7, 146.7, 146.7, 128.6, 127.6, 127.4, 127.4, 125.5, 124.7, 122.7, 113.5, 112.7, 82.6, 80.8, 50.8, 50.6, 40.1, 30.9. HR-MS (ESI) m/z calculated for ($C_{20}H_{23}FN_5$) $[M + H]^+$ 352.1932, found 352.1933. HPLC purity: 95.64%, retention time 4.47 min. C-18 reversed-phase HPLC (Phenomenex, 10 mm × 250 mm); eluent, acetonitrile:H_2O = 50:50; flow rate of 1.0 mL/min.

*(E)-N-((1-(2-Fluoroethyl)-1H-1,2,3-triazol-4-yl)methyl)-4-(4-(ethylamino)styryl)aniline (**22**).* ^{1}H NMR (400 MHz, chloroform-d) δ 7.57 (s, 1H), 7.31 (dd, J = 8.5, 3.6 Hz, 4H), 6.82 (d, J = 1.5 Hz, 2H), 6.64 (d, J = 8.5 Hz, 2H), 6.58 (d, J = 8.5 Hz, 2H), 4.89−4.82 (m, 1H), 4.72 (dd, J = 5.2, 4.0 Hz, 1H), 4.69−4.63 (m, 1H), 4.63−4.56 (m, 1H), 4.49 (s, 2H), 3.18 (q, J = 7.1 Hz, 2H), 1.26 (t, J = 7.1 Hz, 3H). ^{13}C NMR (100 MHz, chloroform-d) δ 147.8, 146.8, 146.65, 128.6, 127.5, 127.4, 127.4, 125.5, 124.6, 122.7, 113.5, 113.0, 82.6, 80.7, 50.9, 50.6, 40.1, 38.7, 15.1. HR-MS (ESI) m/z calculated for ($C_{21}H_{25}FN_5$) $[M + H]^+$ 366.2089, found 366.2089. HPLC purity: 98.41%, retention time 5.05 min. C-18 reversed-phase HPLC (Phenomenex, 10 mm × 250 mm); eluent, acetonitrile:H_2O = 30:70; flow rate of 1.0 mL/min.

*(E)-N-((1-(2-Fluoroethyl)-1H-1,2,3-triazol-4-yl)methyl)-4-(4-(propylamino)styryl)aniline (**23**).* ^{1}H NMR (400 MHz, chloroform-d) δ 7.57 (s, 1H), 7.31 (dd, J = 8.5, 5.1 Hz, 4H), 6.82 (d, J = 1.8 Hz, 2H), 6.65 (d, J = 8.4 Hz, 2H), 6.58 (d, J = 8.5 Hz, 2H), 4.84 (t, J = 4.6 Hz, 1H), 4.76−4.70 (m, 1H), 4.70−4.64 (m, 1H), 4.64−4.58 (m, 1H), 4.49 (s, 2H), 3.10 (t, J = 7.1 Hz, 2H), 1.65 (q, J = 7.2 Hz, 3H), 1.00 (t, J = 7.4 Hz, 3H). ^{13}C NMR (125 MHz, chloroform-d) δ 147.6, 146.6, 146.5, 128.5, 127.3, 127.2, 127.2, 125.4, 124.4, 122.5, 113.3, 112.8, 82.2, 80.8, 50.6, 50.5, 45.8, 39.9, 31.9, 22.7, 11.6. HR-MS (ESI) m/z calculated for ($C_{22}H_{27}FN_5$) $[M + H]^+$ 380.2245, found 380.2248. HPLC purity: 99.93%, retention time 8.13 min. C-18 reversed-phase HPLC (Phenomenex, 10 mm × 250 mm); eluent, acetonitrile:H_2O = 30:70; flow rate of 1.0 mL/min.

*tert-Butyl (4-Formylphenyl)(prop-2-yn-1-yl)carbamate (**24**).* To an oven-dried 100 mL round-bottom flask purged with argon gas and fitted with a magnetic stir bar was added sodium hydride (140 mg, 95%) and *tert*-butyl (4-formylphenyl)carbamate (1.02 g), which was purged with argon gas under dry THF (25 mL) at 0 °C. 3-Bromoprop-1-yne (1.55 mL, 80% in toluene) was added slowly dropwise after 30 min at 0 °C under argon gas. The reaction was stirred under argon and allowed to reach room temperature. After 3 h, the reaction was quenched with water and extracted with ethyl acetate (30 mL × 3). The organic layers were combined and washed twice with water (50 mL) and once with brine (50 mL). The organic layer was dried over Na_2SO_4 and concentrated to give the crude product. Flash chromatography (Hex:EA/8:1) yielded **24** (1.06 g, 89%) as an oil. ^{1}H NMR (400 MHz, chloroform-d) δ 9.92 (s, 1H), 7.87−7.78 (m, 2H), 7.55−7.47 (m, 2H), 4.39 (dd, J = 2.5, 0.9 Hz, 2H), 2.28 (t, J = 2.4 Hz, 1H), 1.46 (s, 9H). ^{13}C NMR (100 MHz, chloroform-d) δ 191.2, 153.1, 147.6, 133.4, 130.2, 125.4, 82.1, 79.4, 72.4, 39.4, 28.2.

*2-Azidoethyl 4-Methylbenzenesulfonate (**25**).* To an oven-dried 100 mL round-bottom flask purged with argon gas and fitted with a magnetic stir bar was added DCM (15 mL), 2-azidoethan-1-ol (2.3 mL, 0.5 M in methyl *tert*-butyl ether), 4-toluenesulfonyl chloride (0.33 g), and Et_3N (0.32 mL). The reaction mixture was allowed to stir overnight at room temperature, and water was then added followed by two extractions with DCM (30 mL). The organic layers were combined and washed with water (50 mL) and brine (50 mL). Flash chromatography (Hex:EA/4:1) yielded **25** (0.22 g, 79%). ^{1}H NMR (400 MHz, chloroform-d) δ 7.85−7.76 (m, 2H), 7.42−7.34 (m, 2H), 4.15 (ddd, J = 5.2, 4.5, 0.9 Hz, 2H), 3.53−3.42 (m, 2H), 2.45 (s, 3H).

Animal Preparation and Studies. All animal experiments were performed in accordance with guidance protocol approved by the Institutional Animal Care and Use Committee (IACUC) of Case Western Reserve University (protocols 2016-0028, 2016-0023). The 8-week old WT C57BL/6 mice were used for all of the in vitro and ex vivo tissue staining. and SD rats (Harlan Laboratory, Indianapolis, IN) and Shiverer mice (Jackson Laboratory, Bar Harbor, ME) were used for microPET/CT imaging studies. The animals were fasted overnight prior to imaging but had access to water. Their diet was then replenished after microPET/CT imaging.

Brain Focal Demyelination Rat Model. Sprague−Dawley female rats (220−250 g, 8 weeks old) were anesthetized and positioned in a stereotaxic frame (Stoelting). A small incision was made in the scalp, and the corpus callosum was targeted using the following stereotaxic coordinates, relative to bregma: anterior−posterior, 0.0 mm; medial−lateral, 2.0 mm; and dorsal−ventral, 3.4 mm. A small hole was drilled in the skull, and a 26S-gauge needle attached to a 10 μL Hamilton Syringe was lowered into the corpus callosum according to the dorsal−ventral coordinate. A microinjector pump (Stoelting) controlled the infusion of 6 μL of lysolecithin (LPC, 0.1% in saline) at a rate of 0.25 μL/min, after which the needle was left in place for 2 min in order to prevent liquid reflux out of the brain parenchyma. The incision was then closed using 5−0 Ethicon sutures, and the animals were allowed to recover on a heating pad. After 5−7 days, the animals were ready for study.

Rat SCI Model. Sprague−Dawley female rats (220−250 g, 8 weeks old) were anesthetized and a restricted laminectomy was conducted to expose the dorsal surface of T13. The vertebral column between T12 and L1 was then stabilized with clamps and forceps fixed to the base of an Infinite Horizon impact device. The midpoint of T13 was impacted with a force of 250 kDyn using a 2.5 mm stainless steel impactor tip, which was used to induce a moderately severe contusive injury to the spinal cord. The musculature was then sutured over the laminectomy site and the skin closed with wound clips followed by subsequent

DOI: 10.1021/acs.jmedchem.6b01328
J. Med. Chem. XXXX, XXX, XXX−XXX

treatment with Marcaine at the incision site. The force/displacement graph was used to monitor impact consistency. After surgery, the animals were carefully monitored daily for pain and body weight with manual bladder expression 2−3 times daily to stimulate reflex voiding until the animals could urinate independently.

In Vitro Tissue Staining of Brain. Wild-type mice (20−22 g, 8 weeks old) were deeply anesthetized and perfused with precooled saline (4 °C, 10 mL/min for 1 min followed by 7 mL/min for 6 min), which was followed by fixation with precooled 4% PFA in PBS (4 °C, 10 mL/min for 1 min followed by 7 mL/min for 6 min). Brain tissues were then removed, postfixed by immersion in 4% PFA overnight, dehydrated in 10%, 20%, and 30% sucrose solution, embedded in a freezing compound (OCT, Fisher Scientific, Suwanee, GA), and sectioned at 20 μm increments with a cryostat (Thermo HM525, Thermo Fisher Scientific Inc., Chicago, IL, USA). To provide staining sections for preliminary FIR measurement, brain sections were collected from AP (1.0) to AP (−0.1), and the first 12 sections were mounted in order on the bottom of 12 superfrost slides (Fisher Scientific) with one section on each slide. Sections 13−24 were mounted in order on the middle of each slide, and sections 25−36 were mounted in order on the top of each slide. Sections were then incubated with tested compounds (1 mM, 5% DMSO in 1× PBS (pH 7.0), 6 sections per compound) for 25 min at room temperature in the dark. Excess compounds were washed by briefly rinsing the slides in PBS (1×) and coverslipped with fluoromount-G mounting media (Vector Laboratories, Burlingame, CA). Sections were then examined under a microscope (Leica DM4000B, Leica Microsystem Inc., Buffalo Grove, IL, USA) equipped for fluorescence (DFC7000T), and images of the stained mouse whole brain sections were acquired with the same exposure time.

FIR Measurement. ImageJ software was used to quantify fluorescent intensity on six sections of each tested compound. A ROI was selected on the genu of the corpus callosum (gcc, white matter), and the same size of ROI was applied on the midline between gcc and the edge of the section (see Figure 2A), which is considered to be gray matter. Images were analyzed by two experienced individuals. The FIR values of white matter to gray matter were then calculated.

Ex Vivo Tissue Staining. Wild-type mice were administered the newly synthesized compounds (40 mg/kg) via tail vein injection, and 30−60 min later the mice were perfused transcardially with saline followed by 4% PFA in PBS. Brains and spinal cords were then removed, postfixed by immersion in 4% PFA overnight, dehydrated in 30% sucrose solution, cryostat sectioned at 100 μm, mounted on superfrost slides, and images were acquired directly using a Leica fluorescent microscope.

In Vitro Staining of Rat Brain Treated with LPC. Five days after surgery, the rats were anesthetized and perfused with saline followed by 4% PFA. Brain tissues were then removed, postfixed in 4% PFA overnight, dehydrated in 10%, 20%, and 30% sucrose solution, embedded in OCT, and sectioned at 20 μm with a cryostat. To determine if the selected compound can differentiate demyelinated regions from normal myelinated sheaths, we conducted in vitro tissue staining using spinal cord sections taken from LPC-treated rats. LPC-treated spinal cord sections were then incubated with tested compounds (1 mM, 5% DMSO in 1× PBS (pH 7.0)) for 25 min at room temperature in the dark. Excess compounds were washed by briefly rinsing the slides in PBS (1×) and coverslipped with fluoromount-G mounting media (Vector Laboratories, Burlingame, CA). Sections were then examined under a microscope (Leica DM4000B, Leica Microsystem Inc., Buffalo Grove, IL, USA) equipped for fluorescence (DFC7000T), and images of the stained mouse whole brain sections were acquired with the same exposure time. In the meantime, standard Luxol-Fast-Blue (LFB) staining was performed on the adjacent LPC-treated spinal cord section for comparison.

Radiosynthesis. No carrier-added (nca) [^{18}F] fluoride was produced by a cyclotron (Eclipse High Production, Siemens) via the nuclear reaction ^{18}O (p,n) ^{18}F. At the end of bombardment (EOB), the activity of aqueous [^{18}F]fluoride (50−100 mCi) was transferred to the GE Tracerlab FXn synthesizer by high helium pressure. After delivery, the radioactive solution was passed through a Sep-Pak light QMA cartridge (Waters, preconditioned with 5 mL of water followed by 10 mL of air in a syringe) and was eluted by K_2CO_3 solution (6 mg in 0.6 mL of water) followed by K_{222} solution (12 mg in 1 mL ofacetonitrile). The solvent was evaporated under a steam of helium at 85 °C for 5 min, and the residue was vacuumed at 55 °C for another 3 min to get the anhydrous K_{222}/[^{18}F] complex. A solution of the tosylated precursors (**25**, 3−5 mg, in 0.5 mL of acetonitrile) was added to the above dried complex, and the mixture was heated at 95 °C for 10 min. Cooling water (10 mL) was then added to the reaction vessel, and the mixture was passed through a C18 plus cartridge and an Oasis HLB plus cartridge in series (Waters, preconditioned with acetonitrile (10 mL), water (10 mL), and followed by air (∼10 mL)). An additional 20 mL of water was used to rinse the reaction vial and the cartridges, followed by air (∼20 mL) to remove the residual water from the HLB cartridge. DMF (400 μL + 500 μL) was used to elute [^{18}F]**26** from the Waters HLB cartridge into a reaction vial prefilled with a mixture of the click reaction precursor **9** (5 mg), 1.25 mg of $CuSO_4{\cdot}5H_2O$, 4 mg of sodium ascorbate, and 3 mg of BPDS in 50 μL (water/DMF = 4/1). The mixture was then stirred for 10 min at 90 °C. After cooling, 0.5 mL of HCl (1 M) was added and the resulting mixture was heated at 90 °C for 10−20 min. A NaOH solution (0.5 mL, 1 M) and water (15 mL) were then added, and the resulting mixture was passed through a preconditioned Sep-Pak C-18 cartridge. The cartridge was then washed with another 20 mL of water, and the crude products were eluted with 1 mL of acetonitrile which was further purified by semipreparative HPLC (Phenomenex C-18, 10 mm × 250 mm; acetonitrile:H_2O = 65:35; flow rate of 3 mL/min). The radioactive fraction containing the desired products was collected, diluted with water, loaded onto a Sep-Pak C-18 cartridge, and eluted with 1 mL of ethanol. After evaporation, the residue was redissolved in 5% ethanol in saline solution and filtered (0.22 μm) into a sterile injection bottle for animal use. RCP and specific activity (SA) were determined by analytical HPLC (Phenomenex C-18; 4.6 mm × 250 mm; acetonitrile:H_2O = 65:35; flow rate of 1 mL/min). SA was calculated from the area of the UV peak of purified F-18 compound and titrated with the standard curve of the nonradioactive reference compound of known concentration.

In Vivo MicroPET/CT Imaging Studies. MicroPET/CT imaging was performed using a Siemens Inveon microPET/CT scanner in the Case Center for Imaging Research. For better anatomic localization, CT coregistration was applied. Before microPET imaging, CT scout views were taken to ensure the brain tissues were placed in the co-scan field of view (FOV) where the highest image resolution and sensitivity are achieved. Under anesthesia, radiotracer was administered via tail vein injection and immediately followed by a dynamic PET acquisition up to 60 min. After the microPET acquisition was done, the rat was moved into the CT field and a two-bed CT scan was performed. A two-dimensional ordered subset expectation maximization (OSEM) algorithm was used for image reconstruction using CT as attenuation correction. For quantitative analysis, the resultant PET images were registered to the CT images, which enabled us to accurately define the ROI and quantify the radioactivity concentrations. In this study, the whole brains of rats were used as ROI and the radioactivity concentrations were determined in terms of SUVs.

Coregistration of in Situ 3D Cryoimaging with PET/CT Imaging. After microPET imaging studies, the rats were administered compound **21** (3−5 mg) via tail vein injection, and 60 min later the rats were perfused transcardially with saline followed by 4% PFA in PBS. Spinal cords were then removed, postfixed by immersion in 4% PFA overnight, dehydrated in 30% sucrose solution, cryostat sectioned at 100 μm, mounted consecutively on superfrost slides, and images were sequentially acquired directly using a Leica fluorescent microscope to give a series of 2D microscopic images along the length of the spinal cord. Slices were aligned sequentially using a semiautomated image registration algorithm. Starting from the first slice image, the current slice was used as the reference image for alignment and the next slice was the floating image. The floating image was aligned via control point pairs between corresponding anatomic features in the two images. A 2D rigid-body transformation (translation, rotation) was used to transform the floating image to

DOI: 10.1021/acs.jmedchem.6b01328
J. Med. Chem. XXXX, XXX, XXX−XXX

align with the reference and a minimum of three control point pairs were used for the transformation. Once two slices were aligned, the algorithm continued with the newly aligned image serving as the reference image and the next slice in the sequence serving as the floating image. All slices in the sequence were aligned by this technique, giving a 3D reconstructed fluorescence image volume. Image volumes from fluorescence, PET, and CT were visualized in Amira using volume rendering and aligned based on the shape of the spine and fiducials from the vertebrae.

In Situ Autoradiography. Wild-type mice were euthanized at 30 min post iv injection of [^{18}F]**21** (111 MBq, 3.0 mCi). The brains were rapidly removed, placed in OCT embedding medium, and frozen at −20 °C. After reaching equilibrium at this temperature, the brains were coronally sectioned at 60 μm on a cryostat and mounted on superfrost slides. After drying by air at room temperature, the slides were put in a cassette and exposed for 20 min to film to obtain images.

■ ASSOCIATED CONTENT

Supporting Information

The Supporting Information is available free of charge on the ACS Publications website at DOI: 10.1021/acs.jmedchem.6b01328.

Additional ^{1}H NMR and ^{13}C NMR spectra for all intermediate and final compounds synthesized; HPLC and HRMS spectra for all of the final compounds (**18**−**23**) (PDF)

PET-CT cryo fusion imaging(AVI)

Molecular formula strings (CSV)

■ AUTHOR INFORMATION

Corresponding Authors

*For C.W.: phone, 216-983-4235; fax, 216-844-8062; E-mail, cxw130@case.edu.

*For Y.W.: phone, 216-844-3288; fax, 216-844-8062; E-mail, yxw91@case.edu.

ORCID

Chunying Wu: 0000-0002-6782-2610

Present Address

¶For Yunjie Zhu: Department of Chemistry and Biochemistry, Oberlin College, Oberlin, Ohio 44074, United States

Notes

The authors declare no competing financial interest.

■ ACKNOWLEDGMENTS

This work is supported in part by the National Multiple Sclerosis Society (RG5174-A-4), Genzyme Corporation, and the Bryon Riesch Paralysis Foundation.

■ ABBREVIATIONS USED

s, singlet; br s, broad singlet; dd, doublet of doublets; ddd, doublet of doublet of doublets; br d, broad doublets; t, triplet; dt, triplets of doublets; q, quartet; m, multiplet; br m, broad multiplet; MS, multiple sclerosis; PET, positron emission tomography; SCI, spinal cord injury; MRI, magnetic resonance imaging; MeDAS, methyl diamino stilbene; TAFDAS, triazole fluorinated diamino stilbene; CNS, central nervous system; DCM, dichloromethane; FIR, fluorescent intensity ratio; ROI, region of interest; gcc, genu of the corpus callosum; BBB, blood−brain barrier; LPC, lysolecithin; LFB, Luxol-Fast-Blue; K_{222}, 4,7,13,16,21,24-hexaoxa-1,10-diazabicyclo[8.8.8]-hexacosane; HPLC, high performance liquid chromography; K_2CO_3, potassium carbonate; BPDS, bathophenanthrolinedisulfonic acid disodium salt; SPE, solid phase extraction; EtOAc, ethyl acetate; MeCN, acetonitrile; EtOH, ethanol; SUV, standardized uptake value; CT, computerized tomography; PFA, paraformaldehyde; FOV, field of view; SAR, structure−activity relationship; TLC, thin-layer chromography; OSEM, ordered subset expectation maximization; RPC, radiochemical purity; SA, specific activity; DMF, dimethylformamide; $NaHCO_3$, sodium bicarbonate; Na_2SO_4, sodium sulfate

■ REFERENCES

(1) Nave, K. A. Myelination and support of axonal integrity by glia. *Nature* **2010**, *468*, 244−252.

(2) Trapp, B. D.; Nave, K. A. Multiple sclerosis: an immune or neurodegenerative disorder? *Annu. Rev. Neurosci.* **2008**, *31*, 247−269.

(3) Compston, A.; Coles, A. Multiple sclerosis. *Lancet* **2002**, *359*, 1221−1231.

(4) Hauw, J. J.; Delaere, P.; Seilhean, D.; Cornu, P. Morphology of demyelination in the human central nervous system. *J. Neuroimmunol.* **1992**, *40*, 139−152.

(5) Hermelinda, S.-C.; Guizar-Sahagun, G.; Feria-Velasco, A.; Grijalva, I.; Espitia, L.; Ibarra, A.; Madrazo, I. Spontaneous long-term remyelination after traumatic spinal cord injury in rats. *Brain Res.* **1998**, *782*, 126−135.

(6) Filippi, M.; Rocca, M. A.; Comi, G. The use of quantitative magnetic-resonance-based techniques to monitor the evolution of multiple sclerosis. *Lancet Neurol.* **2003**, *2*, 337−346.

(7) Leist, T. P.; Marks, S. Magnetic resonance imaging and treatment effects of multiple sclerosis therapeutics. *Neurology* **2010**, *74* (Suppl 1), S54−S61.

(8) Ozturk, A.; Smith, S. A.; Gordon-Lipkin, E. M.; Harrison, D. M.; Shiee, N.; Pham, D. L.; Caffo, B. S.; Calabresi, P. A.; Reich, D. S. MRI of the corpus callosum in multiple sclerosis: association with disability. *Mult. Scler.* **2010**, *16*, 166−177.

(9) Rovaris, M.; Filippi, M. Magnetic resonance techniques to monitor disease evolution and treatment trial outcomes in multiple sclerosis. *Curr. Opin. Neurol.* **1999**, *12*, 337−344.

(10) Frullano, L.; Wang, C.; Miller, R. H.; Wang, Y. A myelin-specific contrast agent for magnetic resonance imaging of myelination. *J. Am. Chem. Soc.* **2011**, *133*, 1611−1613.

(11) Frullano, L.; Zhu, J.; Miller, R. H.; Wang, Y. Synthesis and characterization of a novel gadolinium-based contrast agent for magnetic resonance imaging of myelination. *J. Med. Chem.* **2013**, *56*, 1629−1640.

(12) Frullano, L.; Zhu, J.; Wang, C.; Wu, C.; Miller, R. H.; Wang, Y. Myelin imaging compound (MIC) enhanced magnetic resonance imaging of myelination. *J. Med. Chem.* **2012**, *55*, 94−105.

(13) Wang, C.; Popescu, D. C.; Wu, C.; Zhu, J.; Macklin, W.; Wang, Y. In situ fluorescence imaging of myelination. *J. Histochem. Cytochem.* **2010**, *58*, 611−621.

(14) Wang, C.; Wu, C.; Popescu, D. C.; Zhu, J.; Macklin, W. B.; Miller, R. H.; Wang, Y. Longitudinal near-infrared imaging of myelination. *J. Neurosci.* **2011**, *31*, 2382−2390.

(15) Wang, Y.; Wu, C.; Caprariello, A. V.; Somoza, E.; Zhu, W.; Wang, C.; Miller, R. H. In vivo quantification of myelin changes in the vertebrate nervous system. *J. Neurosci.* **2009**, *29*, 14663−14669.

(16) Wu, C.; Tian, D.; Feng, Y.; Polak, P.; Wei, J.; Sharp, A.; Stankoff, B.; Lubetzki, C.; Zalc, B.; Mufson, E. J.; Gould, R. M.; Feinstein, D. L.; Wang, Y. A novel fluorescent probe that is brain permeable and selectively binds to myelin. *J. Histochem. Cytochem.* **2006**, *54*, 997−1004.

(17) Wu, C.; Wang, C.; Popescu, D. C.; Zhu, W.; Somoza, E. A.; Zhu, J.; Condie, A. G.; Flask, C. A.; Miller, R. H.; Macklin, W.; Wang, Y. A novel PET marker for in vivo quantification of myelination. *Bioorg. Med. Chem.* **2010**, *18*, 8592−8599.

(18) Wu, C.; Zhu, J.; Baeslack, J.; Zaremba, A.; Hecker, J.; Kraso, J.; Matthews, P. M.; Miller, R. H.; Wang, Y. Longitudinal positron emission tomography imaging for monitoring myelin repair in the spinal cord. *Ann. Neurol.* **2013**, *74*, 688−698.

DOI: 10.1021/acs.jmedchem.6b01328
J. Med. Chem. XXXX, XXX, XXX−XXX

(19) Tiwari, A. D.; Wu, C.; Zhu, J.; Zhang, S.; Zhu, J.; Wang, W. R.; Zhang, J.; Tatsuoka, C.; Matthews, P. M.; Miller, R. H.; Wang, Y. Design, synthesis, and evaluation of fluorinated radioligands for myelin imaging. *J. Med. Chem.* **2016**, *59*, 3705−3718.
(20) Glaser, M.; Robins, E. G. 'Click labelling' in PET radiochemistry. *J. Labelled Compd. Radiopharm.* **2009**, *52*, 407−414.
(21) Meldal, M.; Tornoe, C. W. Cu-catalyzed azide-alkyne cycloaddition. *Chem. Rev.* **2008**, *108*, 2952−3015.
(22) Tornoe, C. W.; Christensen, C.; Meldal, M. Peptidotriazoles on solid phase: [1,2,3]-triazoles by regiospecific copper(i)-catalyzed 1,3-dipolar cycloadditions of terminal alkynes to azides. *J. Org. Chem.* **2002**, *67*, 3057−3064.
(23) Tron, G. C.; Pirali, T.; Billington, R. A.; Canonico, P. L.; Sorba, G.; Genazzani, A. A. Click chemistry reactions in medicinal chemistry: applications of the 1,3-dipolar cycloaddition between azides and alkynes. *Med. Res. Rev.* **2008**, *28*, 278−308.
(24) Ding, Y. S.; Lin, K. S.; Logan, J.; Benveniste, H.; Carter, P. Comparative evaluation of positron emission tomography radiotracers for imaging the norepinephrine transporter: (S,S) and (R,R) enantiomers of reboxetine analogs ([^{11}C]methylreboxetine, 3-Cl-[^{11}C]methylreboxetine and [^{18}F]fluororeboxetine), (R)-[^{11}C]-nisoxetine, [^{11}C]oxaprotiline and [^{11}C]lortalamine. *J. Neurochem.* **2005**, *94*, 337−351.
(25) Pagliai, F.; Pirali, T.; Del Grosso, E.; Di Brisco, R.; Tron, G. C.; Sorba, G.; Genazzani, A. A. Rapid synthesis of triazole-modified resveratrol analogues via click chemistry. *J. Med. Chem.* **2006**, *49*, 467−470.
(26) Burley, G. A.; Gierlich, J.; Mofid, M. R.; Nir, H.; Tal, S.; Eichen, Y.; Carell, T. Directed DNA metallization. *J. Am. Chem. Soc.* **2006**, *128*, 1398−1399.
(27) Whiting, M.; Muldoon, J.; Lin, Y. C.; Silverman, S. M.; Lindstrom, W.; Olson, A. J.; Kolb, H. C.; Finn, M. G.; Sharpless, K. B.; Elder, J. H.; Fokin, V. V. Inhibitors of HIV-1 protease by using in situ click chemistry. *Angew. Chem., Int. Ed.* **2006**, *45*, 1435−1439.
(28) Krasinski, A.; Radic, Z.; Manetsch, R.; Raushel, J.; Taylor, P.; Sharpless, K. B.; Kolb, H. C. In situ selection of lead compounds by click chemistry: target-guided optimization of acetylcholinesterase inhibitors. *J. Am. Chem. Soc.* **2005**, *127*, 6686−6692.
(29) Agard, N. J.; Prescher, J. A.; Bertozzi, C. R. A strain-promoted [3 + 2] azide-alkyne cycloaddition for covalent modification of biomolecules in living systems. *J. Am. Chem. Soc.* **2004**, *126*, 15046−15047.
(30) Dishino, D. D.; Welch, M. J.; Kilbourn, M. R.; Raichle, M. E. Relationship between lipophilicity and brain extraction of C-11-labeled radiopharmaceuticals. *J. Nucl. Med.* **1983**, *24*, 1030−1038.
(31) Zhou, D.; Chu, W.; Peng, X.; McConathy, J.; Mach, R. H.; Katzenellenbogen, J. A. Facile purification and click labeling with 2-[^{18}F]fluoroethyl azide using solid phase extraction cartridges. *Tetrahedron Lett.* **2015**, *56*, 952−954.
(32) Bodini, B.; Veronese, M.; Turkheimer, F.; Stankoff, B. Benzothiazole and stilbene derivatives as promising positron emission tomography myelin radiotracers for multiple sclerosis. *Ann. Neurol.* **2016**, *80*, 166−167.
(33) Matias-Guiu, J. A.; Cabrera-Martin, M. N.; Matias-Guiu, J.; Oreja-Guevara, C.; Riola-Parada, C.; Moreno-Ramos, T.; Arrazola, J.; Carreras, J. L. Amyloid PET imaging in multiple sclerosis: an (^{18})F-florbetaben study. *BMC Neurol.* **2015**, *15*, 243.
(34) Burden-Gulley, S. M.; Qutaish, M. Q.; Sullivant, K. E.; Lu, H.; Wang, J.; Craig, S. E.; Basilion, J. P.; Wilson, D. L.; Brady-Kalnay, S. M. Novel cryo-imaging of the glioma tumor microenvironment reveals migration and dispersal pathways in vivid three-dimensional detail. *Cancer Res.* **2011**, *71*, 5932−5940.
(35) Wilson, D.; Roy, D.; Steyer, G.; Gargesha, M.; Stone, M.; McKinley, E. Whole Mouse Cryo-Imaging. *Proc. SPIE* **2008**, *6916*, 69161I−69161I-9.

DOI: 10.1021/acs.jmedchem.6b01328
J. Med. Chem. XXXX, XXX, XXX−XXX